Simulation of DQW GaInNAs laser diodes

J. J. Lim*[1], R. MacKenzie[1], S. Sujecki[1], M. Sadeghi[2], S.M. Wang[2], Y.Q. Wei[2], J.S. Gustavsson[2], A. Larsson[2], P. Melanen[3], P. Sipilä[3], P. Uusimaa[3], A.A. George[4], P.M. Smowton[4], and E.C. Larkins[1]

[1]*School of Electrical and Electronic Engineering, University of Nottingham, Nottingham NG7 2RD, U.K.*

[2]*Photonics Laboratory, Chalmers University of Technology, SE-41296 Göteborg, Sweden*

[3]*Modulight Inc., Hermiankatu 22, FIN-33720 Tampere, Finland*

[4]*Cardiff School of Physics and Astronomy, Cardiff University, Queens Buildings, The Parade, Cardiff, CF24 3AA*

* Corresponding author email: jun.lim@nottingham.ac.uk

Abstract

In this work, the simulation of double quantum well (QW) GaInNAs ridge waveguide (RW) lasers is performed over a wide range of cavity lengths and operating temperatures using a comprehensive in-house 2D laser simulator. The laser simulator takes into account all of the major device physics, including current spreading, capture escape processes, drift diffusion in the QW, 2D optical modes and fully resolved lasing spectra. The gain data used by the simulator was fitted to experimental gain spectra measured by the segmented contact method. The gain model includes the band-anticrossing model for the conduction band and a 4x4 **k·p** model for the valence band. By using a carrier density dependent and temperature dependent linewidth broadening parameter, a good fit with experiment over a temperature range of 300 - 350 K was obtained. A Shockley-Read-Hall lifetime of 0.5 ns and an Auger recombination coefficient of $1x10^{-28}$ cm^6s^{-1} were extracted from the calibration of the laser simulator to experimental device characteristics of broad area (BA) devices. Using the same set of parameters for BA devices, except for a reduced SRH lifetime of 0.45 ns underneath the etch, 2D simulation results were found to agree well with measured RW laser operating characteristics. The impact of the various

recombination processes in the RW laser at threshold has also been identified using the calibrated laser simulator.

1. Introduction

Recently, state-of-the-art GaInNAs edge-emitting lasers (EELs) have demonstrated a great deal of promise as a low-cost replacement for directly-modulated 1.3μm InP devices in access network applications. Lasers based on the GaInNAs/GaAs material system have a large conduction band-offset, which increases the electron confinement and subsequently reduces their temperature sensitivity. These devices have demonstrated a low threshold current density of 300A/cm^2 [1], a high characteristic temperature of up to 200K [2], a 3dB modulation bandwidth of 17GHz at 25°C [3] and are capable of direct modulation up to 10Gb/s at a heat sink temperature of 110°C [4].

In order to further understand and optimize the operating characteristics of these devices, accurate and predictive simulation tools are required. For these tools to be predictive, accurate material parameters are needed. Some of the most essential parameters are the recombination coefficients. Numerous values for the recombination parameters have been previously reported for the dilute nitrides [5] - [8], which have proven useful in assessing the relative contributions of the recombination components. However, most of these reported parameters are extracted based on specific models and assumptions (e.g. the use of *A*, *B* and *C* recombination coefficients and unipolar model) which complicate their use in more general laser simulators. In this paper, we calibrate our in-house laser simulation tool to both experimental gain data and threshold current measurements performed over a range of cavity lengths and temperatures. Through the calibration of the laser simulator, insight can be obtained into the factors determining the performance of the laser.

The paper is organized as follows. In Section 2, a description of the electrical and optical models employed in our in-house 2D laser simulator is provided. The laser structure investigated in this work is then presented in Section 3. This is followed by a description of the bandstructure and gain model used and their calibration to experimental measurements in Section 4. The calibration of the non-radiative material parameters of broad-area and ridge-waveguide devices is presented in Sections 5 and 6, respectively. Finally, an investigation of the temperature behaviour of the various recombination current components at threshold is given in Section 7.

2. Semiconductor laser model

We have developed an in-house 2D laser simulator, which solves the electro-optical problem of the semiconductor laser self-consistently. The lattice heat equation and hence self-heating effect has been ignored, as the main focus of this work was to model the threshold characteristic of the ridge waveguide (RW) laser. However, the temperature dependencies of all the important material parameters are included in order to accurately model the temperature characteristics of the device. The basic semiconductor device equations that describe the electronic behavior of the semiconductor laser have been described in a previous publication [9]. It consists of Poisson's equation and the continuity equations for both bulk and confined electrons and holes. The capture/escape process between the bound and unbound states of the quantum well (QW) is treated as a carrier-carrier scattering process [10] - [12] (a value of 1 ps for the electron and hole capture time has been used for all simulations in this work, although changing the capture time by an order of magnitude was found not to affect the steady-state simulation results). All the relevant recombination processes (i.e. Shockley-Read-Hall (SRH), Auger, spontaneous and stimulated recombination) are included in the continuity equation. The details of the gain and spontaneous emission calculations are presented in Section 4 when the gain and spontaneous emission calculations are fit to experiments.

The semiconductor device equations are supplemented by the photon rate equations, with a separate equation used to solve for the photon population in each longitudinal mode, which has been labeled by the index *l*:

$$v_g(G_l - \alpha_i - \alpha_m)S_l + \beta_{spont,l}^{qw} = 0 , \quad (1)$$

where S_l and G_l are the photon density and modal gain of the longitudinal modes, respectively. v_g is the group velocity, α_i is the internal loss, α_m is the mirror loss and $\beta_{spont,l}^{qw}$ is the spontaneous emission coupled into the cavity mode.

The set of nonlinear partial differential equations given by the basic semiconductor equations are discretized on a 2D (vertical and lateral) non-uniform rectangular grid and are solved self-consistently with the photon rate equations, Eq. (1), using Newton's method. Special care must be taken when solving Eq. (1) by introducing an additional set of "slack variables" and imposing the inequality constraint that $G_l \le \alpha_l - \alpha_m$, as described in [11].

To obtain the transverse optical mode profile of the device, the 2D scalar Helmholtz equation is solved for each longitudinal mode, including the dispersion of the refractive index:

$$\nabla^2\Phi + k_0^2\left[\bar{n}(x,y,\lambda)^2 - \bar{n}_{eff}(\lambda)^2\right]\Phi = 0 , \quad (2)$$

where Φ is the optical mode, k_0 is the propagation constant, $\bar{n}$ is the refractive index, and $\bar{n}_{eff}$ is the effective index of the mode. Eq. (2) is discretized using finite differences and solved for the optical modes using a Rayleigh quotient iteration method. The modal gain, G_l, (needed in Eq. (1)) is calculated using the calculated optical field profile and the following approximation:

$$G_l = \frac{1}{\bar{n}_{eff,0}} \iint \bar{n}_0 |\Phi|^2 g(x,y,\lambda)\, dxdy , \quad (3)$$

where the subscript 0 for the refractive and effective indices indicates the use of unperturbed values (i.e. excluding carrier or temperature induced changes).

The internal loss consists of two components, absorption loss and scattering loss. The scattering loss is treated as a constant, whereas the absorption loss, α_{abs}, is calculated using the following expression:

$$\alpha_{abs} = \frac{1}{\bar{n}_{eff,0}} \iint \bar{n}_0 |\Phi|^2 \left[\sigma_n n(x,y) + \sigma_p p(x,y)\right] dxdy \,, \quad (4)$$

where the local loss is given by the absorption cross-section $\sigma_{n,p}$ multiplied by the carrier densities *n* and *p*.

3. Device structure

The laser structure was grown by molecular beam epitaxy and consists of two 7 nm thick QWs with In concentration of 39% and N concentration of 1.2% separated by 20 nm thick GaAs barrier layers. The 1μm thick cladding layer consists of 50% Al. A graded composition layer of 160 nm thick $Al_xGa_{1-x}As$ ($0.20 \leq x \leq 0.50$), is inserted between the 1μm thick $Al_{0.50}Ga_{0.50}As$ cladding layer and 20 nm thick GaAs separate confinement layer. Further details of the structure and growth conditions are given in [1]. This epitaxial structure was processed to form RW lasers with an etch depth of 1.3 μm and width of 3.4 μm.

4. Gain and spontaneous recombination calibration

In order to calculate the material gain accurately, an accurate calculation of the QW bandstructure is required. The band anticrossing (BAC) model [13] is used for the conduction band, which has been shown to successfully explain the reduction of the bandgap of the dilute nitride material system. (The increase in the electron effective mass is due to both the decreased curvature of the lowest conduction subband and to increased scattering.) A 4x4 **k·p** model, which includes the heavy–hole and light-hole bands, has been used to calculate the valence band dispersion. The spin-orbit split-off band is ignored as they are found to be larger than the valence band offset. In order to obtain quantitative agreement with experiment, band parameter values were taken from the paper by Vurgaftman *et al.* [14]. A value of 70% is used for the band-offset ratio, which gives a conduction band offset of ~400 meV and a valence band offset of ~120 meV. This is in reasonable agreement with recent experimental values from surface

photovoltage measurements [15]. Two additional parameters are required in the BAC model, which are the position of the N level and the coupling parameter V_{MN}. The position of the N level is taken to be 1.65 eV above the valence band maximum of GaAs and V_{MN} is adjusted to have a value of $2.15\sqrt{x}$ eV, where x is the N concentration. These values give agreement with the experimentally observed position of the gain peak. The value of the interaction parameter is within the range of values reported in the literature. The bandstructure of the QW is shown in Fig. 1. Only two subband levels are obtained for both the conduction and valence bands. No light-hole bands were obtained due to the large compressive strain of the device. This causes TE emission to be dominant in these devices. The separation between the subband levels is also large, ~150 meV for the conduction band, which causes the fundamental CB1-HH1 transition to dominate, giving the device a very large optical gain.

To calibrate and verify the gain calculations, the simulations have been compared with experimental measurements obtained using the segmented contact method [16]. Instead of broadening the gain spectra directly, the broadened spontaneous emission spectrum was calculated first and the following equation was used to obtain the gain spectrum from the spontaneous emission spectrum [17]:

$$g(E) = \frac{3\pi^2 \hbar^3 c^2}{2\bar{n}^2 E^2} R_{spon}(E)\left[1-\exp\left(\frac{E-\Delta E_F}{kT}\right)\right], \tag{5}$$

This method was found to eliminate the unphysical absorption tail at low energy commonly obtained when broadening the gain spectra directly and also ensures that the gain passes through zero exactly at the quasi-Fermi level separation energy. The spontaneous emission spectrum was broadened using a hyperbolic secant lineshape function [18]:

$$L(E-\hbar\omega) = \frac{\tau_{in}}{\pi\hbar}\operatorname{sech}\left(\frac{E-\hbar\omega}{\hbar/\tau_{in}}\right), \tag{6}$$

This lineshape function was found to give better agreement with experiment due to the exponential decay in the wings compared to the broader Lorentzian linewidth broadening

function. The intraband relaxation lifetime was taken to vary as a function of carrier density and temperature as follows:

$$\tau_{in} = (1.95 \times 10^{-13} - 4 \times 10^{-16} T) \cdot \left(n/10^{18}\right)^{-1/2} \text{ s}, \quad (7)$$

where T is in Kelvin and the carrier density n is in cm^{-3}. The $n^{-1/2}$ dependence of τ_{in} has been taken from a model of lifetime broadening by Kucharska *et al.* [19] and the variation with temperature is obtained from fitting the simulated spectra to experimental data. As can be seen in Fig. 2, good agreement with the experimental data was obtained over a range of bias levels and temperatures.

It is noted that inhomogeneous broadening of the band edge states due to fluctuations in QW width and composition is typically represented by a Gaussian broadening function. By performing a series expansion, the sech function can be shown to be equivalent to a Gaussian function up to second-order approximation, with the width of the Gaussian function broader than the sech function by a factor of $\sqrt{2}$. At typical lasing carrier densities of 2 x 10^{18} cm^{-3} and at 300 K, the intraband relaxation time given by Eq. (7) is 75 fs or 12.4 meV. This is equivalent to a Gaussian linewidth of 17.6 meV, which is within the range of values reported in the literature (e.g. 17 meV was reported by Thränhardt *et al.* [20] and 11 meV by Park [21]).

The temperature dependence of the broadening parameter of 0.09 meV/K given by Eq. (7) is well within the range of values reported in the literature. Previous work by Tomic *et al.* [22] used a temperature dependent broadening parameter of 0.039 meV/K over the range 30 K to 300 K, whereas Fehse *et al.* [5] used a temperature dependent broadening parameter of 0.22 meV/K over the range 300 K to 370 K. Nevertheless, when comparing to these values, it must be kept in mind that they are quoted over different temperature ranges, neglect the carrier dependence of the broadening parameter and in the case of [5], employs a different line broadening function.

The agreement between simulation and experiment can be observed more clearly from Fig. 3, which shows a plot of the peak modal gain vs. quasi-Fermi level separation. Although the

quasi-Fermi level separation gives an indication of the carrier population in the device, it is still not possible to extract the carrier densities experimentally. However, from the bandstructure of the device, the carrier density in the QW can be calculated giving us the plot of peak material gain vs. carrier density as shown by Fig. 4. It is noted that although the electron and hole carrier densities in the QW are assumed equal in Fig. 4 for illustrative purposes, no assumption of charge neutrality in the QW is made in the laser simulator. It is also well known that the gain vs. carrier density relation can be well represented by the logarithmic function $g = g_{0N}\ln(n/n_{tr})$. By fitting the simulated curves using the logarithmic function, the gain coefficients and transparency carrier densities are extracted for temperatures of 300 – 350 K as shown in Table 1.

Because it is too numerically intensive to calculate the gain and spontaneous emission directly at each spatial position and bias in the laser simulator, the gain and spontaneous emission spectra have been tabulated as a function of electron and hole carrier densities, wavelength and temperature which can be accessed later by the laser simulator.

5. Non-radiative recombination calibration

Having calibrated the gain, spontaneous emission and the absorption cross-section, the important parameters to calibrate next are the non-radiative recombination parameters. To do this, 1D (vertical) simulations were used to model the dependence of the peak modal gain vs. current density as obtained using the segmented contact method. Lateral current spreading, which occurs almost exclusively in the p-GaAs contact layer, in the segmented contact device has been taken into account to estimate the current density. From measurements of the nearfield emission between 300 - 350 K, the current spreading is estimated to be 5 μm on either side of the 50 μm stripe giving a total width of 60 μm over the full range of current density used here. Note: the different sections of the multisection device are electrically isolated by etching through the p-metallisation and highly doped p-contact layer. Assuming that the CHSH Auger process is dominant for long wavelength materials, good agreement was found using an Auger

coefficient of $1x10^{-28}$ cm^6s^{-1} and a SRH lifetime of 0.5 ns in the QW. As can be seen in Fig. 5, the agreement between the simulated gain vs. current density is reasonably good for modal gains less than ~30 cm^{-1}. At higher modal gains, the experimental gain increases less rapidly with current density compared to simulation. This is especially apparent at a temperature of 350K. However, self-heating effects can be ruled out as the experimental measurements have been performed under pulsed conditions. Hole leakage from the QW has been considered in the capture/escape model, as the escape time of carriers has an exponential dependence with temperature similar to a thermionic emission model. The discrepancy could be due to some other thermally activated leakage process which has not been included in the model and is the subject of further work.

The SRH recombination lifetime extracted in this work is found to be in excellent agreement with the carrier lifetime of 0.5 ns obtained from time-resolved photoluminescence measurements of similar GaInNAs material at room temperature [23]. Slightly higher values of 0.9 ns [5] and 1.3 ns [6] have also been reported in the literature for the SRH recombination lifetime. The difference between the extracted value in this work and that reported in [5] and [6] could be due to differences in the measurement and extraction technique as well as due to the composition and growth method/conditions employed. For example in [5], the spontaneous recombination is assumed to be proportional to n^2 whereas in this work, the simulated spontaneous recombination was found to be better represented by an $n^{1.8}$ dependence. Due to the larger spontaneous recombination using the n^2 dependence, the reported SRH recombination lifetime in [5] could be overestimated. As for the device studied in [6], a different growth technique (MOCVD) was used, tensile strained barriers were employed and a lower N content (0.5%) was incorporated in the QW. All these differences could potentially result in a different SRH lifetime to the device studied in this work. As for the Auger coefficient, the extracted value is found to be at the centre of the range of values previously reported for the GaInNAs material

system. For example, Auger coefficient values of $3.3x10^{-29}$ cm^6s^{-1} [8], $4x10^{-29}$ cm^6s^{-1} [5], $2.2x10^{-28}$ cm^6s^{-1} [7] and $3.1x10^{-28}$ cm^6s^{-1} [6] have been reported in the literature.

6. Ridge waveguide laser simulation

Although most of the important material parameters have been determined in Sections 4 and 5, many parameters still remain to be determined in the laser simulator for each layer in the laser structure. The number of independently adjustable parameters was reduced as much as possible by using values reported in the literature. Table 2 gives some of the important parameters for each layer of the device at room temperature. The bandgap energy varies as a function of temperature and is taken from Vurgaftman *et al.* [13], which is consistent with the values used in the bandstructure calculation. The mobilities are taken from [24], which includes their dependence on doping and temperature. A low electron mobility value of $500cm^2/Vs$ has been used for the GaInNAs QW, consistent with experimental observations [25]. Although there is uncertainty over its exact value, it was found that the electron mobility of the QW only weakly affects the simulated threshold current. For the refractive index dispersion, the model given by Afromowitz [26] is used, which shows good agreement with experiment in the near bandgap region. The refractive index value for the GaInNAs QW was taken from [27].

As for the internal loss, a value of ~10 cm^{-1} was obtained from measurements using the segmented contact method. However, it is difficult to separate the relative contributions of absorption and scattering loss to the internal loss due to the lack of knowledge of absorption loss, in particular intervalence band absorption (IVBA), in the dilute nitride material system. However, from experimental gain measurements of a similar $In_{0.35}Ga_{0.65}As/GaAs$ multiple QW laser [28], the internal loss was shown to increase by around 6 cm^{-1} over a current range of 4 mA. This increase with injection current would seem to indicate that IVBA is still significant in this material system. By setting the scattering loss to zero and setting the absorption cross section for holes to a value of 2×10^{-16} cm^2, an internal loss of ~10 cm^{-1} was obtained at

threshold, in agreement with device measurements. Simulations were also repeated where IVBA was set to zero with the scattering loss set to 10 cm^{-1} and it was found that the threshold current varied by a maximum of 1.8 mA over the entire range of cavity lengths and temperature. Hence, regardless of the origin of the internal loss, the simulated results are still in agreement with measurements within the experimental uncertainty (standard deviation of ~2mA over a range of devices).

The threshold current of RW lasers was simulated using our in-house 2D laser simulator, using material parameters determined from literature and calibrated to experiment. Using the SRH recombination lifetime of 0.5 ns determined from the 1D calibration, the graph of threshold current vs. temperature for cavity lengths of 300, 500, 1000 and 1500 μm was obtained as shown in Fig. 6. There is a small discrepancy between simulation and experiment, with the simulated values generally lower than the experimental values. The 'missing' current seems to be proportional to the length, suggesting there is a leakage current density which has not been taken into account in the simulation. Observing the SEM image of the device, which has been digitized in Fig. 7, it can be seen that the etch has gone very close to the active region. This could very well increase the threshold current due to the increased defects in the QW induced by the plasma damage from the etching process or equally likely, the etch could have gone into the QW, increasing the surface recombination. If the SRH recombination lifetime is decreased from 0.5 ns to 0.45 ns in the region $|x|>3$ μm (i.e. where the etched surface is close to the active region), better agreement is obtained between the simulated and measured threshold characteristic, as shown in Fig. 8.

The L-I curves are plotted in Fig. 9 for different cavity lengths at temperatures of (a) 25°C and (b) 75°C. As can be seen, the agreement in the threshold current and slope efficiency at low bias is reasonably good. At higher biases, however, the experimental L-I curves begin to roll-over due to self-heating effects, which was not included in these simulations.

7. Investigation of recombination processes

An investigation of the variation of the different recombination mechanisms in the device at threshold has also been performed. By integrating the individual recombination mechanisms over the volume of the device, the variation of the current components at threshold vs. temperature can be obtained, as shown in Fig. 10 for cavity lengths of (a) 300 μm and (b) 1500 μm. It is noted that the SRH, spontaneous and Auger recombination components are presented only for the QW and the total barrier recombination is presented as a separate component. For both lengths, it can be seen that SRH recombination makes the largest contribution to the threshold current. It is also the least temperature sensitive of all the recombination mechanisms and explains the high characteristic temperature of these devices. This is in agreement with previous investigations of recombination mechanisms in dilute nitride lasers [5] - [8].

8. Conclusion

The gain and spontaneous emission calculation has been calibrated to experimental data measured using the segmented contact method. The broad area segmented contact device was modelled using 1D simulations. From the simulations, the Auger recombination coefficient and SRH recombination lifetimes were determined by fitting to the experimental data of peak modal gain vs. current density. The ridge waveguide structure was then simulated using a 2D laser model. The simulation results of the ridge waveguide lasers were found to be in good agreement with experiment in terms of the threshold current vs. temperature dependence for a range of cavity lengths. To obtain this agreement, a reduced SRH lifetime was introduced in the region where the etch was close to the active region. In agreement with previous investigations of recombination processes in dilute nitride lasers, it was found that SRH recombination dominates the threshold current and contributes to the high characteristic temperature of the device.

9. Acknowledgments

The authors gratefully acknowledge the support of the European Commission through the FP6 IST project FAST ACCESS (IST-004772).

10. References

[1] Y.Q. Wei, M. Sadeghi, S.M. Wang, P. Modh, and A. Larsson, “High performance 1.28 μm GaInNAs double quantum well lasers,” Electron. Lett., Vol. 41, No. 24, pp. 1328–1329, 2005.

[2] Y.Q. Wei, J.S. Gustavsson, M. Sadeghi, S.M. Wang, A. Larsson, P. Savolainen, P. Melanen, and P. Sipilä, “Uncooled 2.5 Gb/s operation of 1.3 μm GaInNAs DQW lasers over a wide temperature range,” Opt. Exp., Vol. 14, No. 7, pp. 2753–2759, 2006.

[3] Y.Q. Wei, J.S. Gustavsson, M. Sadeghi, S.M. Wang, A. Larsson, “Dynamics and temperature-dependence of 1.3-μm GaInNAs double quantum-well lasers,” IEEE J. Quantum Electron., Vol. 42, No. 12, pp. 1274-1280, 2006.

[4] J.S. Gustavsson, Y.Q. Wei, M. Sadeghi, S.M. Wang, and A. Larsson, “10 Gb/s modulation of 1.3 μm GaInNAs lasers up to 110 ºC,” Electron. Lett, Vol. 42, No. 16, pp. 925–926, 2006.

[5] R. Fehse, S. Tomic, A.R. Adams, S.J. Sweeney, E.P. O'Reilly, A. Andreev and H. Riechert, "A quantitative study of radiative, Auger, and defect related recombination processes in 1.3-μm GaInNAs-based quantum-well lasers," IEEE J. Sel. Topics Quantum Electron, Vol. 8, No. 4, pp. 801-810, 2002.

[6] O. Anton, C.S. Menoni, J.Y. Yeh, L.J. Mawst, J.M. Pikal and N. Tansu, "Increased Monomolecular Recombination in MOCVD Grown 1.3-μm InGaAsN–GaAsP–GaAs QW

Lasers From Carrier Lifetime Measurements," IEEE Photon. Technol. Lett., Vol. 17, No. 5, pp. 953-955, 2005.

[7] J. Hader, J.V. Moloney, and S.W. Koch, "Microscopic Evaluation of Spontaneous Emission- and Auger-Processes in Semiconductor Lasers," IEEE J. Quantum Electron., Vol. 41, No. 10, pp. 1217-1226, 2005.

[8] A. D. Andreev and E. P. O'Reilly, "Theoretical study of Auger recombination in a GaInNAs 1.3 μm quantum well laser structure," Appl. Phys. Lett., Vol. 84, No. 11, pp. 1826-1828, 2004.

[9] J.J. Lim, T.M. Benson, and E.C. Larkins, "Design of wide-emitter single-mode laser diodes," IEEE J. Quantum Electron., Vol. 41, No. 4, pp. 506-516, 2005.

[10] B. Romero, J. Arias, I. Esquivias, and M. Cada, "Simple model for calculating the ratio of the carrier capture and escape times in quantum-well lasers," Appl. Phys. Lett., Vol. 76, No. 12, pp. 1504-1506, 2000.

[11] M.A. Alam, M.S. Hybertsen, R.K. Smith, G.A. Baraff, "Simulation of semiconductor quantum well lasers," IEEE Trans. Electron Devices, Vol. 47, No. 10, pp. 1917-1925, 2000.

[12] B. Witzigmann, A. Witzig, and W. Fichtner, "A multidimensional laser simulator for edge-emitters including quantum carrier capture," IEEE Trans. Electron Devices, Vol. 47, No. 10, pp. 1926-1934, 2000.

[13] J. Wu, W. Shan and W. Walukiewicz, "Band anticrossing in highly mismatched III-V semiconductor alloys," Semicond. Sci. Technol., Vol. 17, No. 8, pp. 860-869, 2002.

[14] I. Vurgaftman and J.R. Meyer, and L.R. Ram-Mohan, "Band parameters for III-V compound semiconductors and their alloys," J. Appl. Physics, Vol.89, No. 11, pp. 5815-5875, 2001.

[15] M. Galluppi, L. Geelhaar, H. Riechert, "Band offsets analysis of dilute nitride single quantum well structures employing surface photo voltage measurements," J. Electron. Materials, Vol. 35, No. 4, 2006.

[16] P. Blood, G.M. Lewis, P.M. Smowton, H. Summers, J. Thomson and J. Lutti, “Characterization of semiconductor laser gain media by the segmented contact method,” IEEE J. Select. Topics Quantum Electron., Vol. 9, No. 5, pp. 1275-1282, 2003.

[17] G.M. Lewis, P.M. Smowton, J.D. Thomson, H.D. Summers and P. Blood, “Measurement of true spontaneous emission spectra from the facet of diode laser structures,” Appl. Phys. Lett., Vol. 80, No. 1, pp. 1-3, 2002.

[18] W.W. Chow and S.W. Koch, *Semiconductor-Laser Fundamentals*, Berlin, Germany: Springer-Verlag, 1999.

[19] A.I. Kucharska and D.J. Robbins, ”Lifetime broadening in GaAs-AlGaAs quantum well lasers,” IEEE J. Quantum Electron., Vol. 26, No. 3, pp. 443-448, 1990.

[20] A. Thranhardt, I. Kuznetsova , C. Schlichenmaier, S.W. Koch, L. Shterengas, G. Belenky, J.Y. Yeh, L.J. Mawst, N. Tansu, J. Hader, J.V. Moloney, W.W Chow, "Nitrogen incorporation effects on gain properties of GaInNAs lasers: Experiment and theory," Appl. Phys. Lett., Vol. 86, No. 20, 201117, 2005.

[21] S.H. Park, ”Intraband relaxation time in InGaNAs quantum-well lasers and comparison with experiment,” Phys. Status Solidi B, Vol. 242, No. 5, pp.1022-1026, 2005.

[22] S. Tomic, E.P. O'Reilly, R. Fehse, S.J. Sweeney, A.R. Adams, A.D. Andreev, S.A. Choulis, T.J.C. Hosea and H. Riechert, "Theoretical and experimental analysis of 1.3-μm InGaAsN/GaAs lasers," IEEE J. Select. Topics Quantum Electron., Vol. 9, No. 5, pp. 1228-1238, 2003.

[23] A. Kaschner, T. Luttgert, H. Born, A. Hoffmann, A.Y. Egorov and H. Riechert, "Recombination mechanisms in GaInNAs/GaAs multiple quantum wells," Appl. Phys. Lett., Vol. 78, No. 10, pp. 1391-1393, 2001.

[24] V. Palankovski and R. Quay, *Analysis and Simulation of Heterostructure Devices*, Wien, New York: Springer-Verlag, 2004.

[25] R. Mouillet, L.A. de Vaulchier, E. Deleporte, Y. Guldner, L. Travers, J.C. Harmand, “Role of nitrogen in the mobility drop of electrons in modulation-doped GaAsN/AlGaAs heterostructures,” Solid State Commun., Vol. 126, No. 6, pp. 333-337, 2003.

[26] M.A. Afromowitz, “Refractive index of $Ga_{1-x}Al_xAs$,” Solid State Comm., Vol. 15, pp. 59-63, 1974.

[27] T. Kitatani, M. Kondow, K. Shinoda, Y. Yazawa, M. Okai, “Characterization of the refractive index of strained GaInNAs layers by spectroscopic ellipsometry,” Jpn. J. Appl. Phys., Vol. 37, No. 3A, pp. 753-757, 1998.

[28] A. Schonfelder, J.D. Ralston, K. Czotscher, S. Weisser, J. Rosenzweig and E.C. Larkins, "Optical gain and spontaneous emission in InGaAs/GaAs multiple quantum well laser diodes," J. Appl. Phys., Vol. 80, No. 1, pp. 582-584, 1996.

Table I Extracted gain coefficient and transparency carrier density for three different temperatures.

Temperature	g_{0N} (cm^{-1})	N_{tr} ($10^{18}cm^{-3}$)
300 K	3151	1.37
325 K	3005	1.53
350 K	2781	1.67

Table 2 Selected physical parameters of laser structure.

Layer	Thickness (μm)	E_g (eV)	μ_n (cm^2/Vs)	μ_p (cm^2/Vs)	$\bar{n}$
p-GaAs	0.10	1.42248	1309	42.2	3.41741
p-$Al_{0.50}Ga_{0.50}As$ (cladding)	1.00	2.08076	196	77.7	3.15105
$Al_{0.50\text{-}0.20}Ga_{0.50\text{-}0.80}As$ (graded)	0.16	2.08076 - 1.72303	809 - 2875	181 - 253	3.15105 - 3.30392
$Ga_{0.61}In_{0.39}N_{0.012}As$ (QW)	0.007	1.00797	500	483	3.60
GaAs (barrier & SCL)	0.020	1.42248	7800	490	3.41741
$Al_{0.20\text{-}0.50}Ga_{0.80\text{-}0.50}As$ (graded)	0.16	1.72303 - 2.08076	2875 - 809	253 - 181	3.30392 - 3.15105
n-$Al_{0.50}Ga_{0.50}As$ (cladding)	1.00	2.08076	196	77.7	3.15105
n-GaAs	0.30	1.42248	1851	51	3.41741

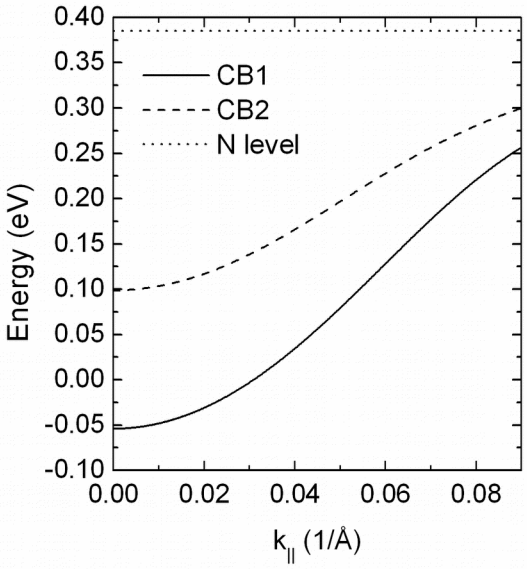

(a)

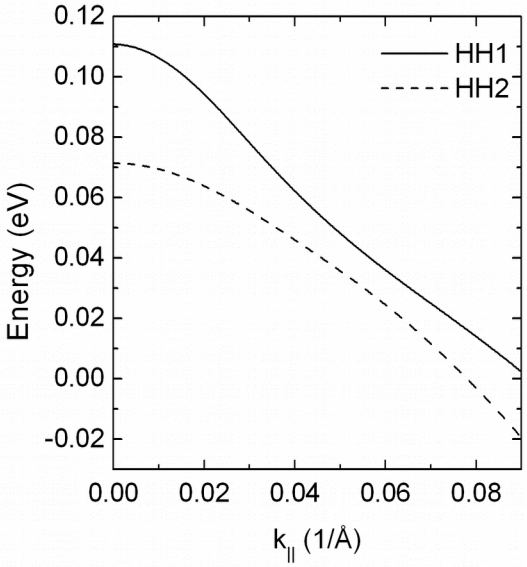

(b)

Fig. 1 (a) Conduction band and (b) valence band structure of $Ga_{0.61}In_{0.39}NAs/GaAs$ QW.

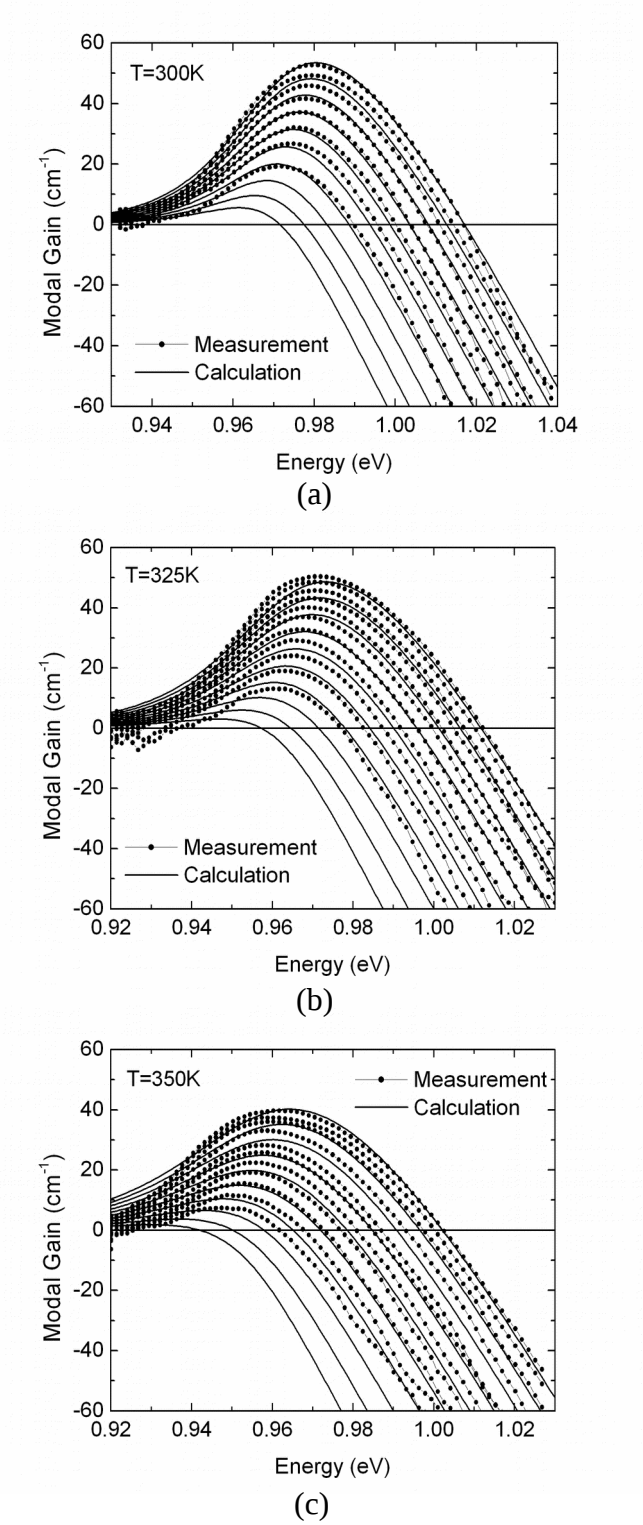

Fig. 2 Measured and calculated gain spectra of $Ga_{0.61}In_{0.39}NAs/GaAs$ laser structure for various bias levels and at temperatures of (a) 300K, (b) 325K and (c) 350K.

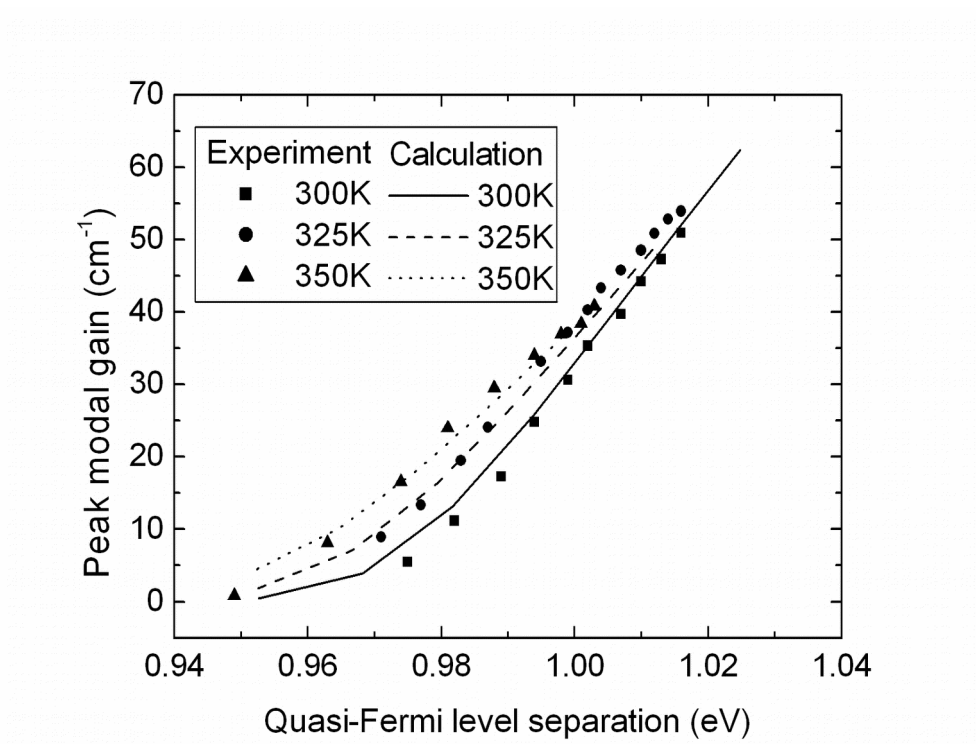

Fig. 3 Calculated and measured peak modal gain vs. Fermi-level separation for temperatures of 300K, 325K and 350K.

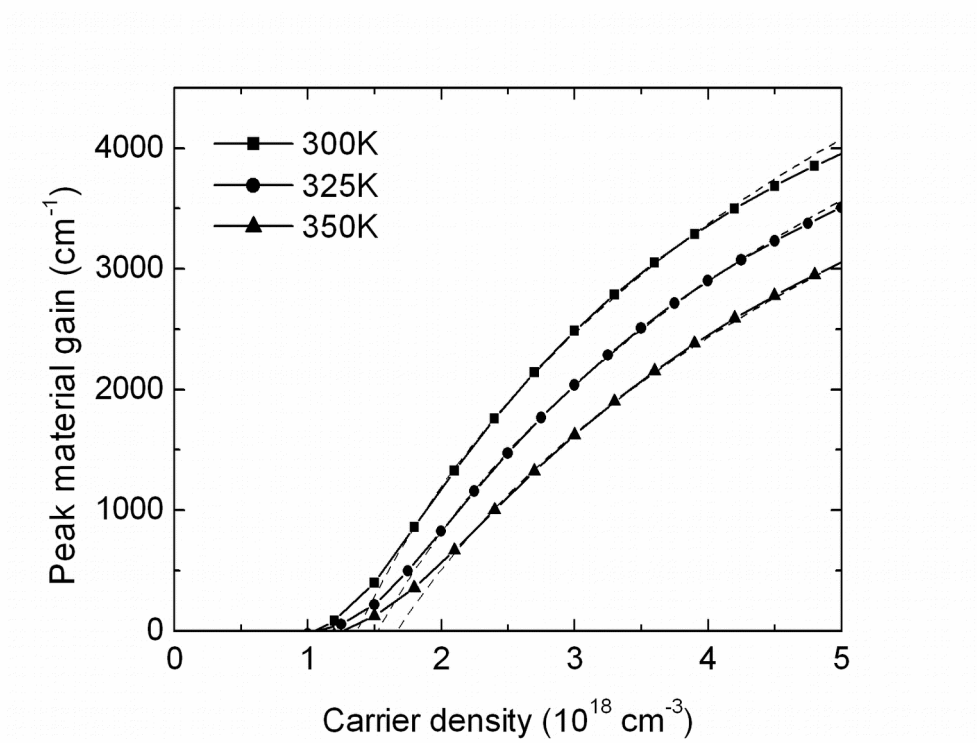

Fig. 4 Calculated peak material gain vs. carrier density for temperatures of 300K, 325K and 350K. The dashed lines are fits to logarithmic function.

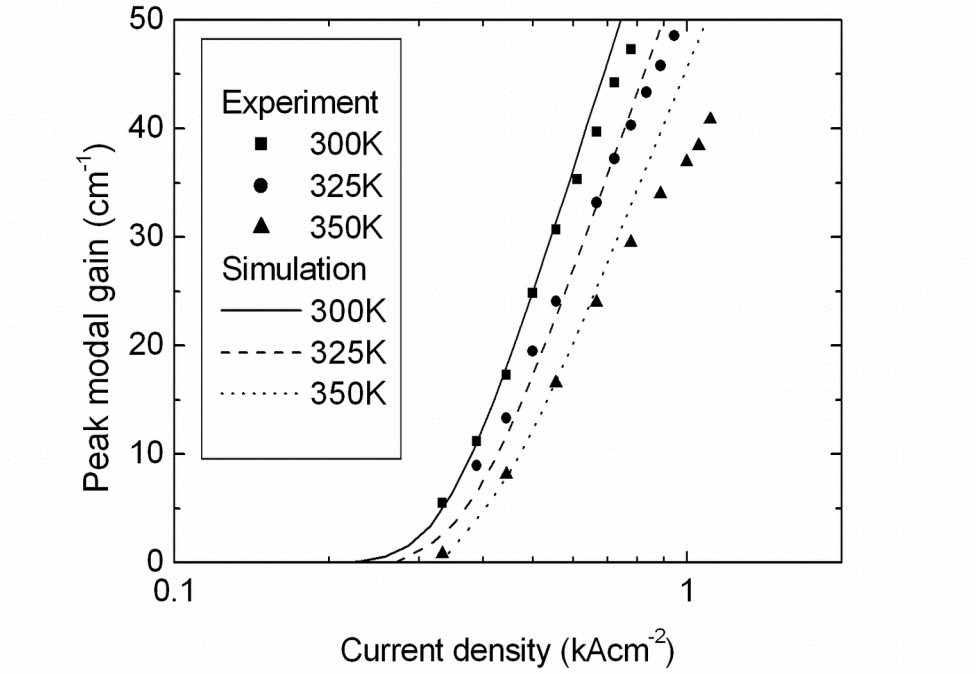

Fig. 5 Simulated and measured peak modal gain vs. current density of a broad area device for temperatures of 300K, 325K and 350K.

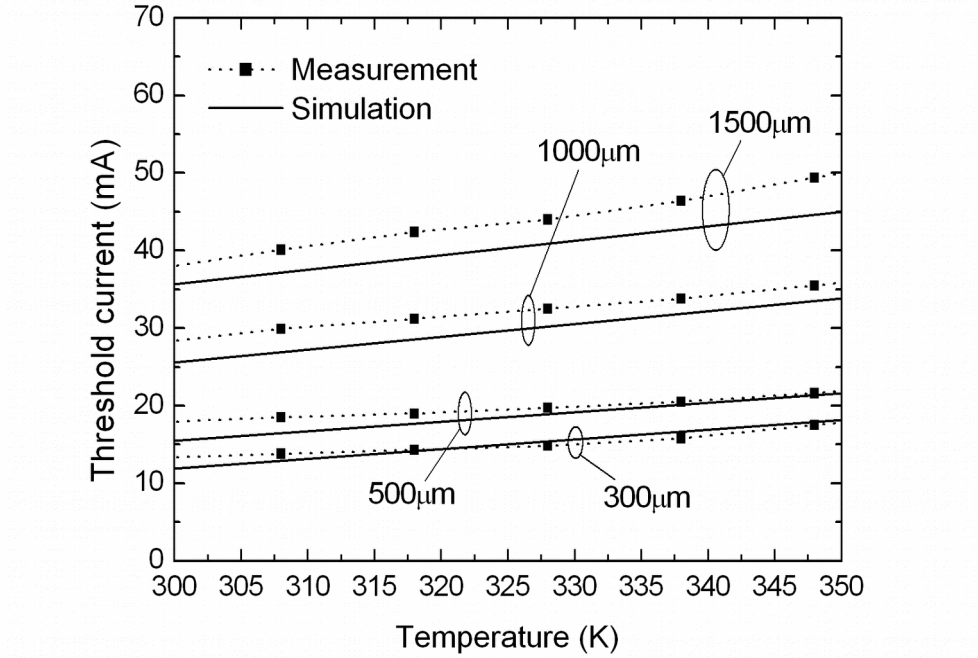

Fig. 6 Measured and simulated threshold current vs. temperature for RW laser cavity lengths between 300-1500μm. Simulation results using $\tau_n = \tau_p = 0.5$ns throughout the QW.

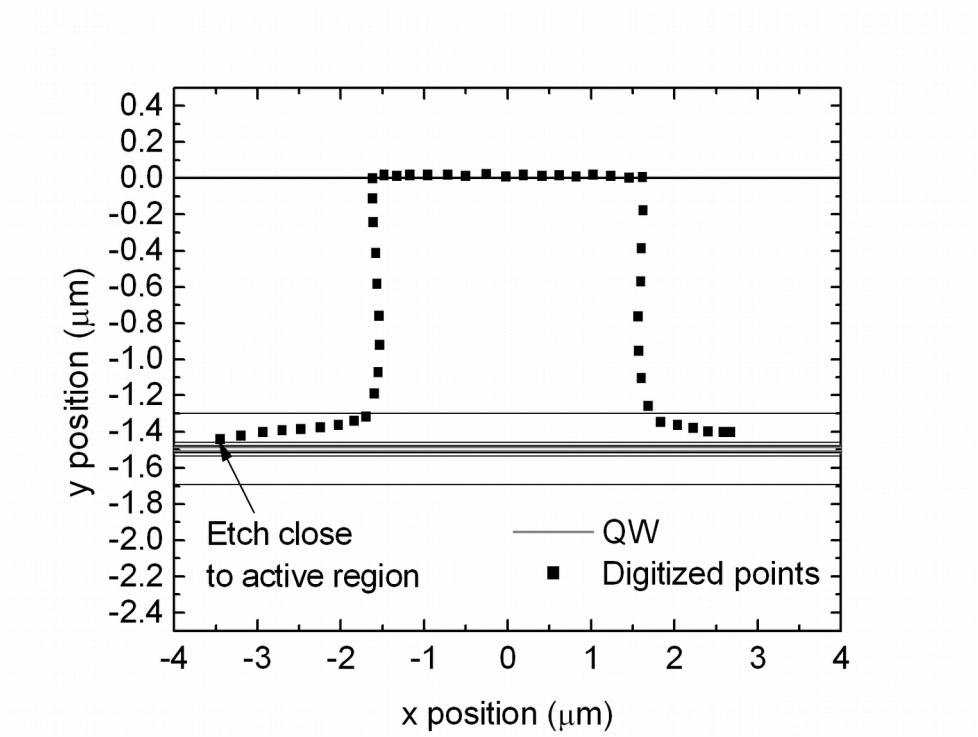

Fig. 7 Digitized plot of SEM image with QW indicated illustrating the deep etch close to the active region.

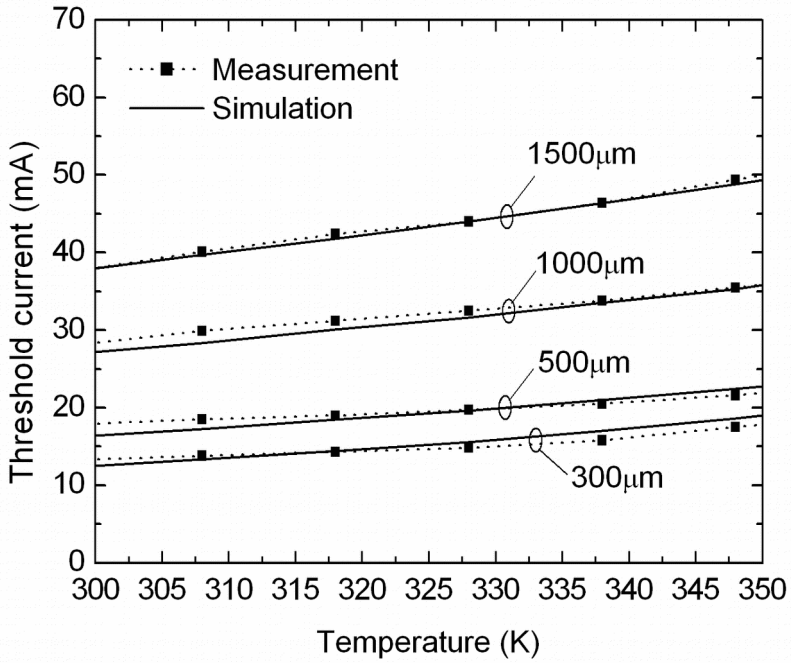

Fig. 8 Measured and simulated threshold current vs. temperature for RW laser cavity lengths between 300-1500μm. Simulation results using reduced SRH lifetime of $\tau_n = \tau_p = 0.45$ns for $|x| > 3\mu$m.

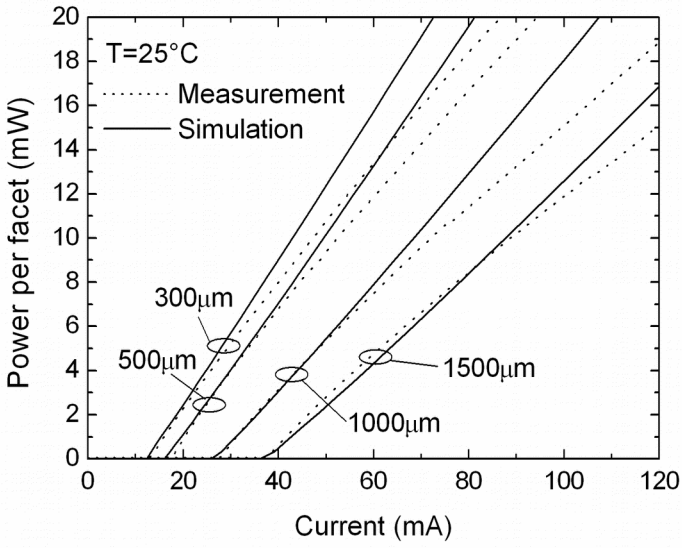

(a)

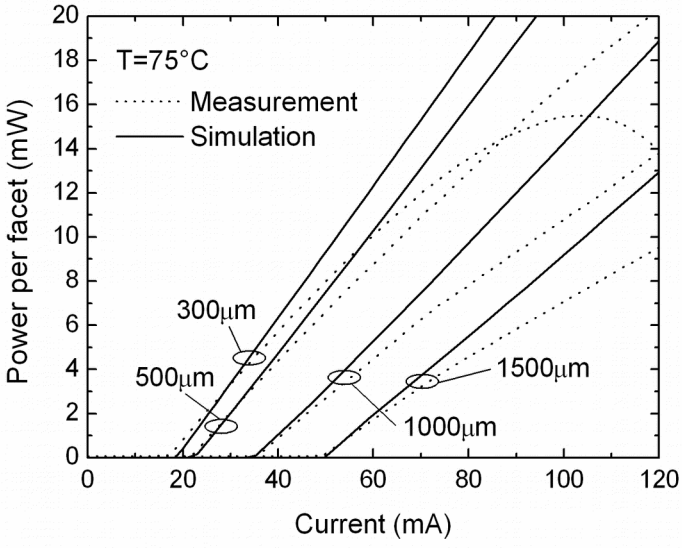

(b)

Fig. 9 L-I curves of RW lasers with different cavity lengths at a temperature of (a) 25°C and (b) 75°C.

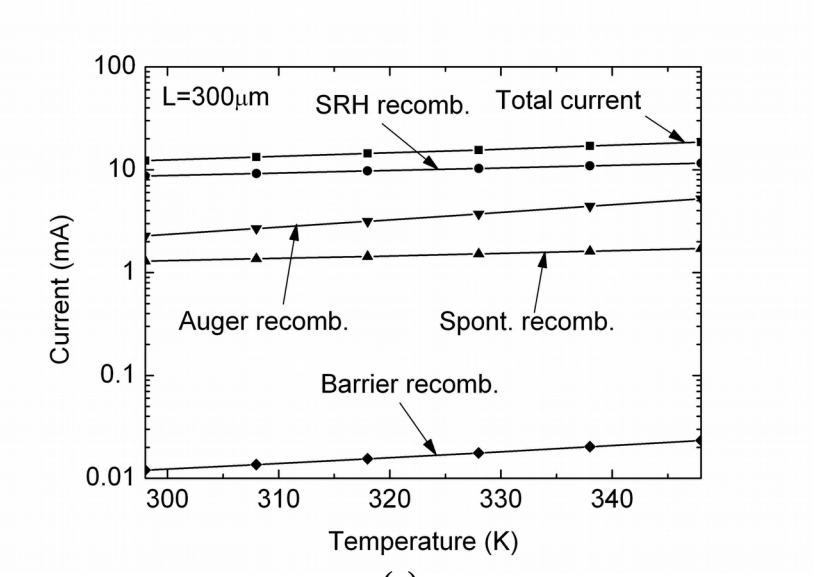

(a)

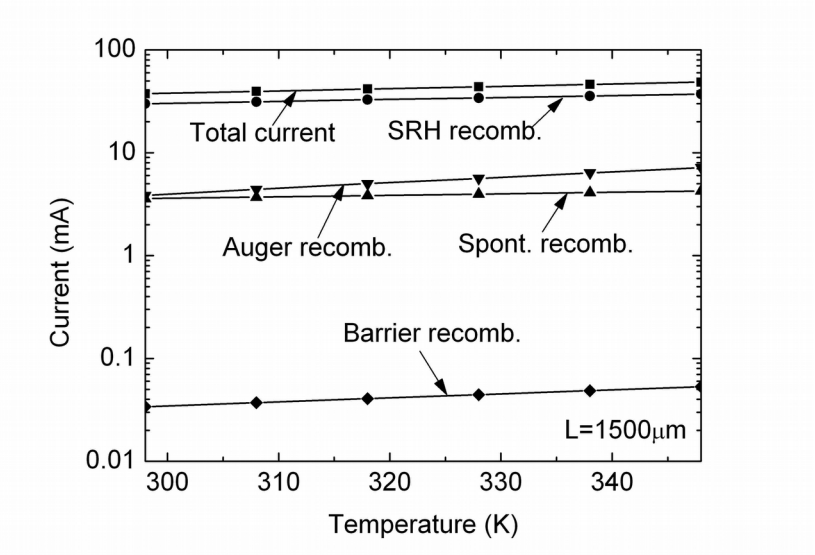

(b)

Fig. 10 Threshold current components as a function of temperature for RW laser with cavity length of (a) 300μm and (b) 1500μm.